metals

MDPI

Article

The Effects of Microstructure on the Thermophysical Properties of the K439B Ni-Based Superalloy

Yidong Wu, Jiemin Gao, Xuanjing Zhang, Jiahui Zheng and Xidong Hui *

State Key Laboratory for Advanced Metals and Materials, University of Science and Technology Beijing, Beijing 100083, China
* Correspondence: xdhui@ustb.edu.cn

Abstract: The thermophysical properties of superalloys are critical for the design, fabrication, and service of hot-end components in engines. In this work, the influence of microstructure on the thermophysical parameters including heat conductivity, thermal diffusivity, heat expansion coefficient, and specific heat capacity of the K439B superalloy, which is a prospective cast superalloy for engine casings, were investigated from 100 °C to 900 °C. It has been observed that these properties increase with temperature, especially between 700 °C and 800 °C, for alloys subjected to different heat treatment processes. When compared under the same temperature, these parameters decrease with an increase in the size and volume fraction of the γ' phase in the alloys. Meanwhile, the interfaces between the γ/γ' phase and the boundaries between dendrites also impeded the heat treatment. It can be concluded that among the alloys with different heat treatment process, the sequence 1160 °C/4 h + 1080 °C/4 h + 845 °C/20 h exhibited the most stable heat conductivity and lowest heat expansion coefficient, making it advantageous for high-temperature service.

Keywords: K439B Ni-based superalloy; heat treatment; γ' phase; thermophysical properties

Citation: Wu, Y.; Gao, J.; Zhang, X.; Zheng, J.; Hui, X. The Effects of Microstructure on the Thermophysical Properties of the K439B Ni-Based Superalloy. *Metals* **2024**, *14*, 1074. https://doi.org/10.3390/met14091074

Academic Editor: Marcello Cabibbo

Received: 23 July 2024
Revised: 9 September 2024
Accepted: 14 September 2024
Published: 19 September 2024

1. Introduction

Ni-based superalloys are widely used in hot-end components such as aerospace, gas turbines, and automobiles due to their excellent high-temperature strength and structural thermal stability [1–5]. The thrust and fuel economy required for advanced aircraft engines are strongly dependent on and further limited by the operating temperature of components used in the hot end [6,7]. Therefore, the research and development of high-performance superalloys has long been at the forefront in the field of materials. The K439B cast Ni-based superalloy, developed by the Beijing Institute of Aeronautical Materials Research of China Aerospace Development Corporation, has excellent mechanical properties at high temperatures, long-term structural stability, and casting and welding properties. It is very promising for use in the manufacture of engine casings with an operating temperature of 800 °C and above.

When referring to the casting process design and microstructure control of the engine casings, the thermophysical properties of superalloys, such as specific heat capacity, thermal conductivity, thermal diffusivity, and the coefficient of thermal expansion, must be taken into consideration. The thermophysical properties also play a crucial role in the safety, stability, and thermal efficiency of the engine during service [8–10]. The coefficient of thermal expansion is critical for components that need to take thermal expansion into account, ensuring that the component expands and contracts properly as the temperature changes, and to avoid damage resulting from thermal expansion mismatches. The thermal diffusivity affects the rate of heat transfer in nickel-based superalloys over temperature gradients. Rapid heat transfer is able to maintain temperature equilibrium and prevent overheating that can lead to degradation or damage to the alloy. The specific heat capacity is an index to assess the material's ability for heat storing. Superalloys with a high specific

heat capacity are able to store more heat and thus withstand temperature shocks while the aircraft enters and leaves the atmosphere. Alloys with excellent thermal conductivity dissipate heat evenly during solidification and processing, which is favorable for reducing frictional heat generated at the contact interface, reducing adhesion and abrasive wear and thus improving wear resistance, while reducing the thermal stress on the alloy matrix to improve its fatigue resistance. For superalloys' service at extreme temperatures (higher than 800 °C) and other relatively harsh tribological conditions, it is not enough to rely only on their own thermal conductivity, and a further deposition of self-lubricating material coatings on their surface to reduce wear and friction is required [11]. In addition, the changes in phase composition and microstructure of the alloy can be deduced by the variation of the thermophysical properties with temperature. Therefore, the determination and evaluation of thermophysical properties are critical for the development of new high-temperature alloys. K439B alloy is a new alloy that can be used at 800 °C. Present research on this alloy mostly focuses on strength and welding performance. Its microstructural stability at 800 °C has been explored by some researchers, including the evolution of microstructure and related mechanical properties at ambient temperature. Liu et al. [12] found that the γ' phase coarsened with increasing aging time at 800 °C, leading to a decrease in both tensile strength and elongation. Zhang et al. [13] investigated the evolution of microstructure, mechanical properties, and stress rupture life at 815 °C/379 MPa of a K439B alloy aged at 800 °C for up to 3000 h, and found that the size of γ' phase increased, the movement of dislocations was dominated by the formation of stacking faults through cutting into the γ' phase, and both tensile strength at ambient temperature and the stress rupture life were gradually decreased with a prolongation of the aging time. In addition, some researchers have also investigated the welding properties of this alloy. Li et al. [14] conducted laser welding experiments on the K439B alloy to study the effect of post-weld heat treatment on the microstructure and mechanical properties of the joints. However, there were few reports on the variation of high-temperature thermophysical properties with temperature, as well as the correlation between the microstructure and thermophysical properties of the alloy. Hence, this article focuses on the changes of the thermal diffusion, thermal expansion, specific heat capacity, and thermal conductivity in the K439B superalloy with different microstructural characteristics in the temperature range of 100 °C–900 °C. The correlation between the microstructure and thermophysical properties is analyzed, and the obtained results should contribute theoretically not only to guide the modulation of microstructure and properties, but also to the design, manufacture, and service of casing components.

2. Materials and Methods

The cast Ni-based superalloy K439B, with equiaxed grains used for the tests, consists of the elements Ni, Co, Cr, Al, W, Ti, Ta, Nb, C, and B in the range of compositions shown in the literature [12–15], which includes 19.1 wt.% Co, 22.4 wt.% Cr, 4.3 wt.% W + Ta + Nb, 5.1 wt.% Al + Ti, 0.12 wt.% C, and Ni in balance. The alloy was fabricated by vacuum melting and precision casting. The heat treatment of the casting specimens was performed in a non-vacuum heat treatment furnace (Nabertherm GmbH, Bremen, Germany) using three different schedules, as shown in Figure 1. The H1 treatment consisted of homogenization at 1160 °C for 4 h followed by cooling to room temperature, further heating to 1080 °C, then holding for 4 h. The process of H2 was held at 845 °C for 10 h after H1 treatment, while H3 was held at 845 °C for 20 h after H1 treatment. All heat treatments were ramped up at 10 °C/min to the specified temperature and air-cooled to room temperature followed by each hold. And specimens for the thermophysical properties test were machined into different cylinders. The cylinders with diameter 12.5 mm and height 2.5 mm ($\varphi 12.5 \times 2.5$) are used to measure heat conductivity and thermal diffusivity, $\varphi 6 \times 20$ to measure the average coefficient of linear expansion, and $\varphi 3 \times 1$ to measure heat capacity. The equilibrium phase diagram of the K439B alloy was calculated using Thermo-Calc software (2024b, Royal Institute of Technology, Stockholm, Sweden) utilizing the TTNi8 thermodynamic database.

Chemical and electrolytic etching were carried out using HNO_3:HF:$C_3H_8O_3$ = 1:2:1 (volume ratio) and H_3PO_4:HNO_3:H_2SO_4 = 3:10:12 (volume ratio) solutions for the metallographic sample preparation, respectively. Microstructure characterization was carried out using a scanning electron microscopy (SEM, ZEISS SUPRA 55, Zeiss, Oberkochen, Germany). The room temperature phase composition of all specimens was analyzed by X-ray diffraction (XRD, D8 Advance, Bruker AXS SE, Karlsruhe, Germany) using Cu Kα radiation. The size and volume fraction of the γ′ phase located in the dendrite core in microstructure photographs taken by SEM was statistically analyzed by Image Pro Plus software (6.0, Media Cybernetics, Rockville, MD, USA), and 5 fields of view were selected to obtain the average value. Thermal conductivity and thermal diffusivity were measured using a laser thermal conductivity meter (TA DLF-1600, TA Instruments, New Castle, DE, USA). The specimens were sprayed with graphite, dried, and then placed into the crucible sample holder of the laser thermal conductivity meter for testing. The system was evacuated and then the experiment was conducted in a nitrogen-protective atmosphere. The specific heat capacity was measured by a differential scanning calorimeter (Netzsch STA-449C, Netzsch, Bavaria, Germany), of which the specimens were placed flat into a platinum–rhodium crucible. After vacuum purification, three high-temperature experiments, baseline, baseline + sample, and baseline + sample test, were performed under the protective atmosphere of argon (flow rate of 25 mL/min, gas purity > 99.99%). The average coefficient of linear expansion was measured using a dilatometer (Netzsch DIL 402SU, Netzsch, Bavaria, Germany). Measurements were carried out under a protective atmosphere of argon (flow rate of 50 mL/min) in the temperature range of 25–900 °C at a rate of 5 K/min.

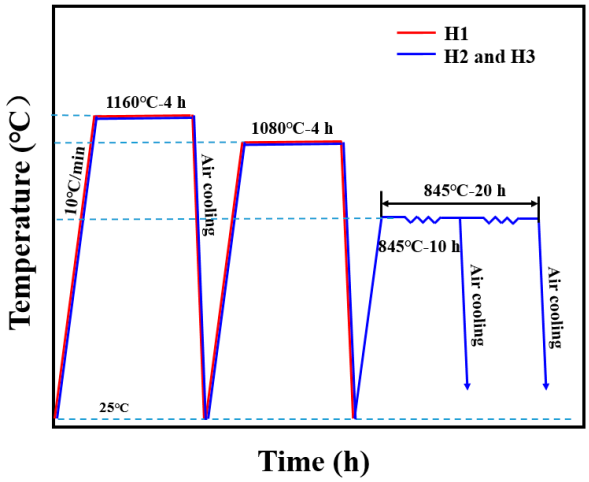

Figure 1. Schematic diagrams of three different heat treatment schedules for the K439B alloy.

3. Results

3.1. Effect of Heat Treatment on Microstructure

Figure 2 shows the microstructure of an as-cast K439B alloy, which consists of the γ phase matrix, γ′ phase precipitation strengthened phase, γ + γ′ eutectic phase, η-phase and, MC-type carbides. The γ′ phase with the shape of granules is diffusely distributed in the matrix. Most precipitates in the dendritic core exhibit near-spherical shapes and a small amount of irregular shapes, as shown in Figure 2a, and their average particle diameter is ~60 nm. Meanwhile, the γ′ phase in the interdendritic region presents an irregular flower-like shape, as shown in Figure 2b, with an average size of ~185 nm. The (γ + γ′) eutectic phase precipitates from the liquid during the solidification of the alloy, and it mainly exists in the dendrite core, presenting a petal-like shape, as shown in Figure 2c. MC-type carbides, rich in Ti, Ta, and Nb, are formed in the late stage of solidification, and they are distributed in the interdendritic region and at the grain boundaries, as shown in Figure 2d. In addition, a small amount of needle-like η phase is observed in the interdendritic region in Figure 2e,f.

The equilibrium phase diagram of the K439B alloy obtained by Thermo-Calc thermodynamic calculation software is shown in Figure 3a, where the γ' phase is dissolved in the γ matrix in the temperature range of 1070 °C–1300 °C. When the temperature is lower than 1070 °C, the γ' phase precipitates from the supersaturated γ matrix. Figure 3b shows the XRD patterns of the alloys under three different heat treatment conditions, revealing that the microstructure of all three alloys consists of the γ matrix, γ' phase, and MC-type carbides at room temperature. As shown in Figure 4, $M_{23}C_6$-type carbides, with much smaller sizes than MC-type carbides, are also presented at the grain boundaries. The interdendritic region and grain boundaries of the equiaxed cast Ni-based superalloy K439B will enrich in Ti, Ta, Nb, and other elements during the solidification process, which leads to nucleation and the growth of MC carbides. The MC carbides at the grain boundaries usually degrade during the aging process [16], resulting in a combination of C and Cr in the matrix to form $M_{23}C_6$ carbides. Therefore, both MC and $M_{23}C_6$ carbides existed at the grain boundaries, while only MC carbides are presented in the interdendritic region (inside the grains), as shown in Figure 4. Additionally, Figure 4 also reveals that the amount of $M_{23}C_6$ carbides at the grain boundaries increased with the extension of the aging time.

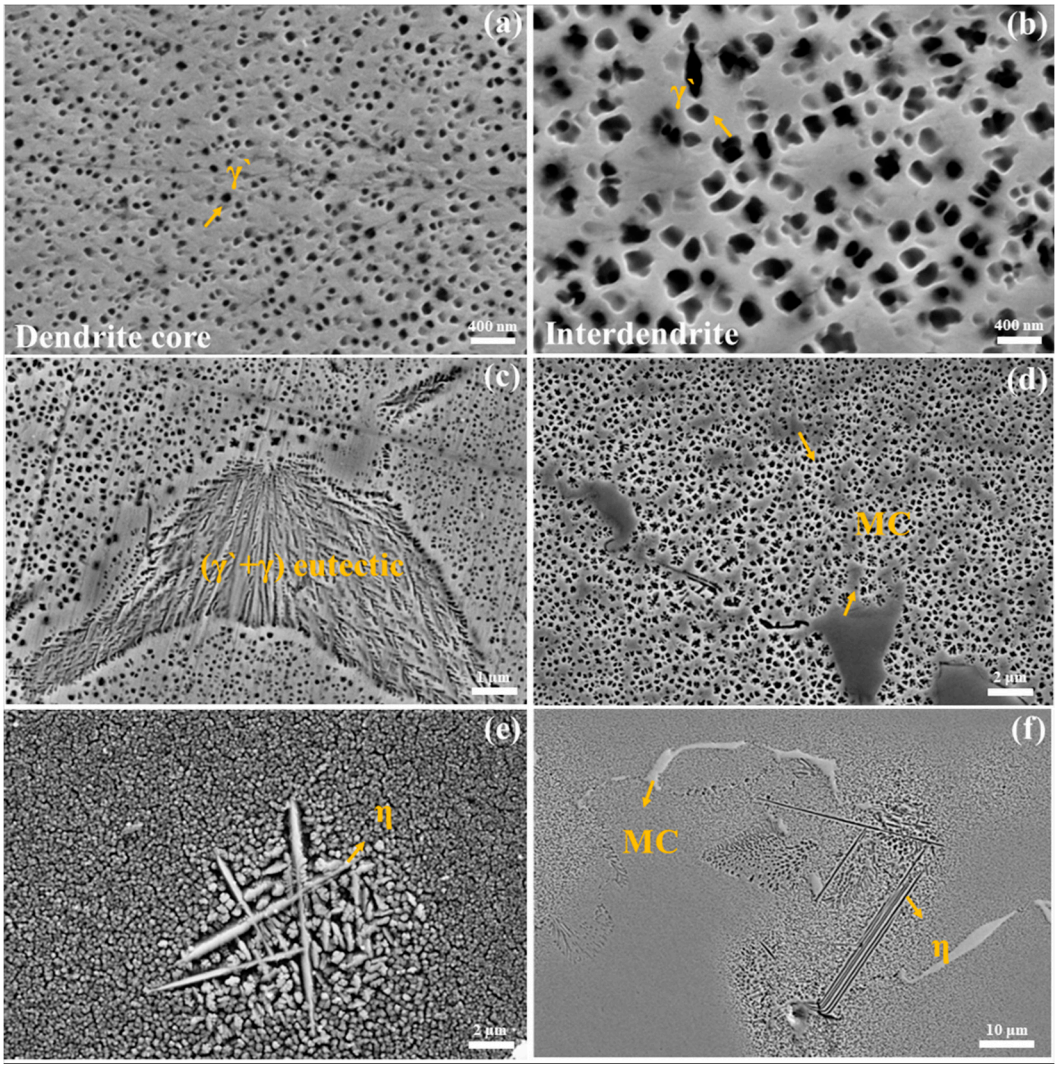

Figure 2. The SEM morphology of an as-cast K439B alloy. (**a**) The γ' phase in the dendrite core; (**b**) the γ' phase in the interdendrite region; (**c**) γ' + γ eutectic; (**d**) MC-type carbides; (**e**) the η phase at high magnification; and (**f**) the η phase at high magnification.

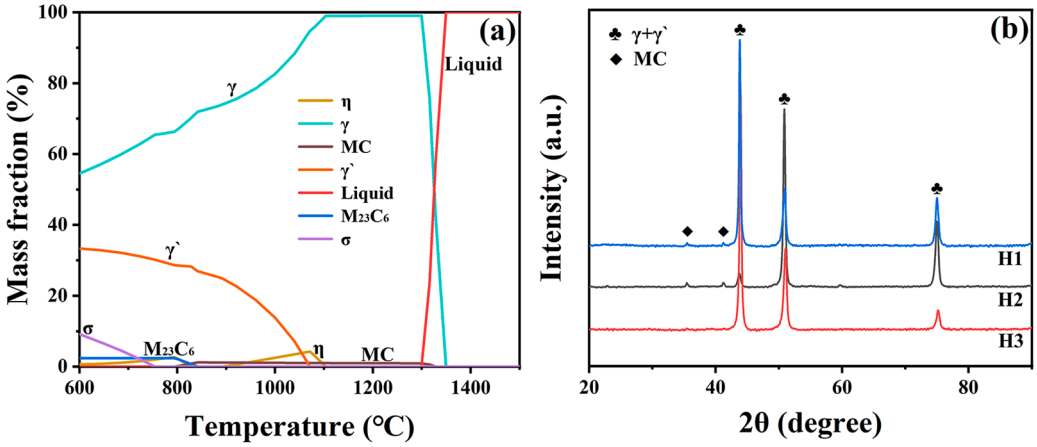

Figure 3. (**a**) The equilibrium phase diagram of the K439B alloy calculated by Thermo-Calc software and (**b**) the XRD patterns of three alloys with different heat treatment processes.

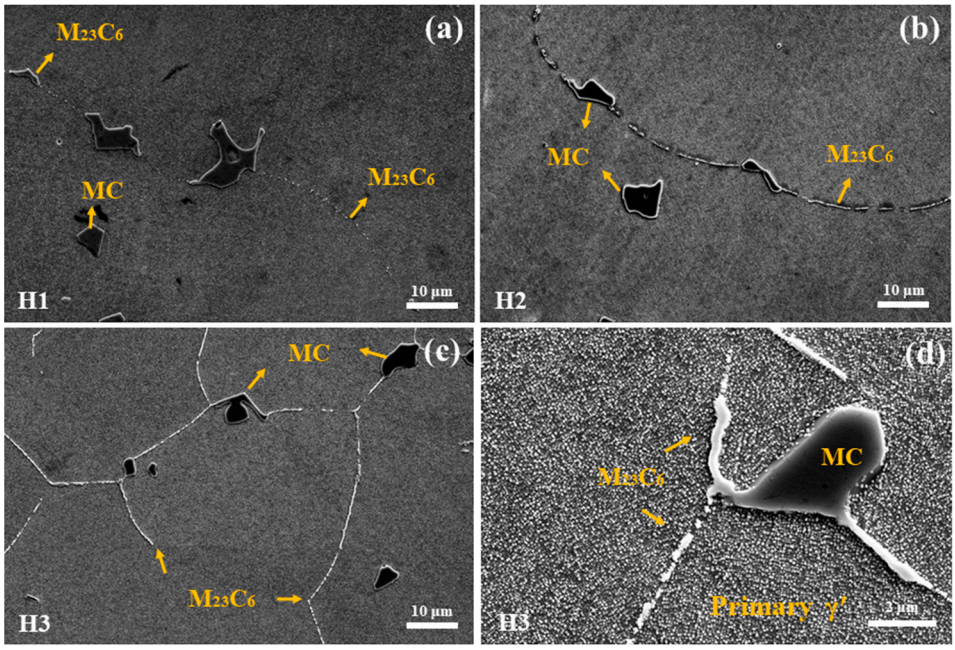

Figure 4. SEM morphology of carbides at grain boundaries and within grains: (**a**) H1; (**b**) H2; (**c**) H3; and (**d**) high-magnification image of H3.

The γ′ phases of the as-cast K439B superalloy were back dissolved into the matrix through the homogenization treatment in the H1 heat treatment regime, but they inevitably precipitated again during the air-cooling process [17]. There exist two different types of γ′ phase distributions in the H1 specimens. The fine spherical γ′ phase located in the dendrite core region is uniformly distributed in the γ matrix, as shown in Figure 5d. The γ′ phase in the interdendritic region has a dimorphic distribution, i.e., there are two kinds of γ′ phases with distinct sizes distributed in the interdendritic region, as shown in Figure 5a–c. A dimorphic distribution can be obtained after utilizing sub-solid solution treatments at a temperature lower than that required for a complete solid solution. This results from the incomplete dissolution of the primary γ′ phase during sub-solid solution treatment and a finer secondary γ′ phase precipitation during the cooling process [18,19]. Additionally, the dimorphic distribution of the γ′ phase result from the precipitation of secondary γ′ phase during the subsequent cooling process of the solid solution treatment. The γ′ phases with varying sizes formed during the two-stage aging process also lead to the γ′ phase dimorphic distribution, even though the primary γ′ phases were completely dissolved

during homogenization. Moreover, different cooling rates also affect the generation of the dimorphic γ′ phase in addition to the heat treatment temperature.

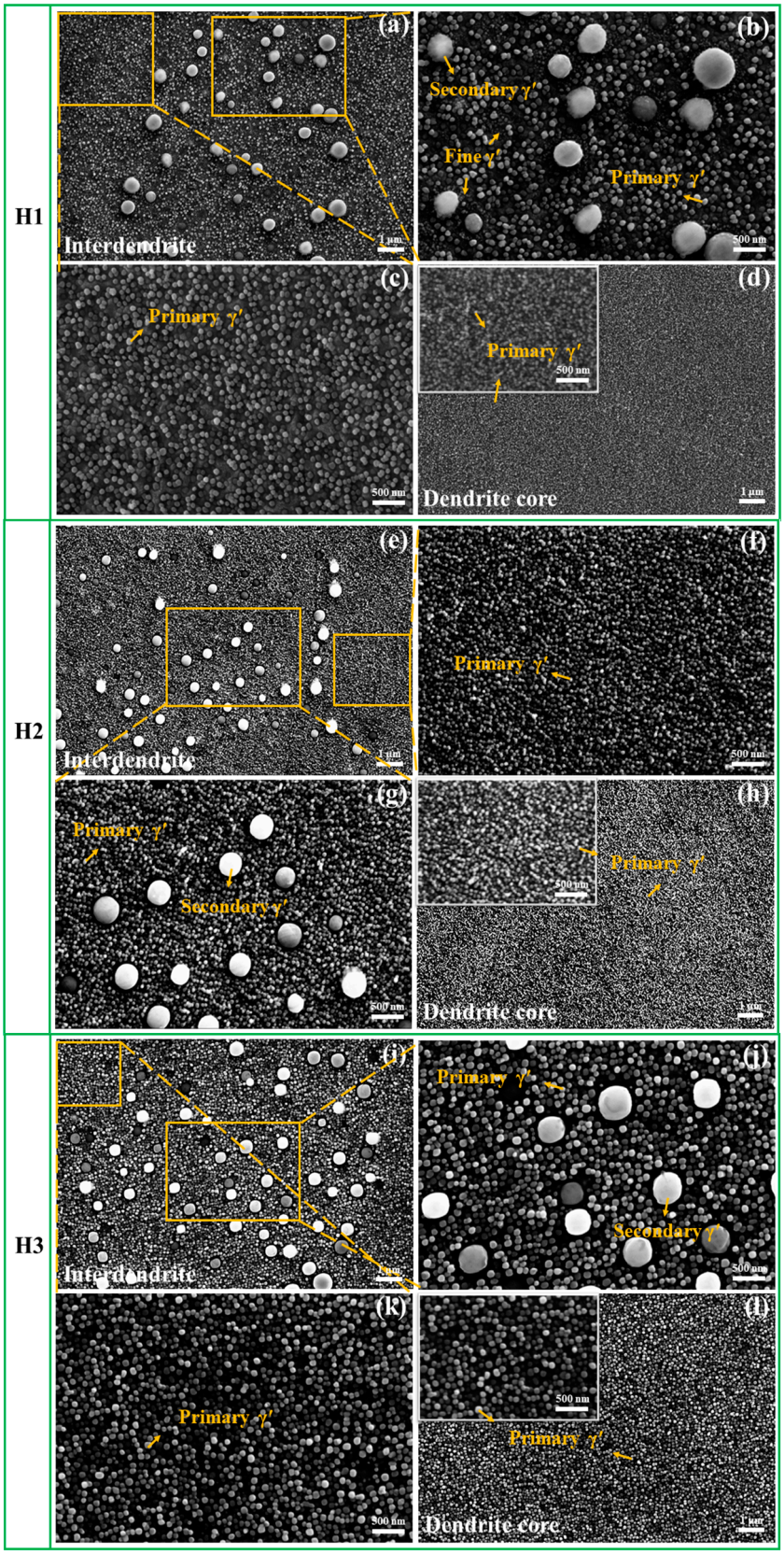

Figure 5. SEM morphology of γ′ phase and γ matrix: (**a**–**d**) H1; (**e**–**h**) H2; and (**i**–**l**) H3 heat treatment.

On the basis of H1, H2 and H3 added an aging treatment at 845 °C. The large secondary γ′ phases located in interdendritic region showed no significant change in size with the extension of aging time, which can be revealed from the comparison of Figure 5a,e,i, while the fine primary γ′ phases became larger to some extent, as shown in Figure 5b,g,j. Similarly, the fine primary γ′ phases in the dendrite core grew as the holding time extended at 845 °C, according to the comparison of Figure 5d,h,l. The equivalent diameter and area fraction of the primary γ′ phase in the dendrite core of the alloys after the three heat treatments are counted, and the statistical results are shown in Figure 6. The area fraction can be used to represent the volume fraction because of the homogeneous distribution of the γ′ phase in this region. According to Figure 6, the γ′ phase with an equivalent diameter of 28.79 ± 1.28 nm is uniformly distributed in the matrix with a volume fraction of 14.34 ± 2.00% after H1 treatment. Whereas, after holding at 845 °C for 10 h (H2), the size and volume fraction of the γ′ phase increases to 37.22 ± 0.98 nm to 18.99 ± 1.01%, respectively. The γ′ phase continues to grow with the aging time, and after aged for 20 h (H3), the size increases to 56.82 ± 2.06 nm, and the volume fraction also reaches to 20.76 ± 0.43%.

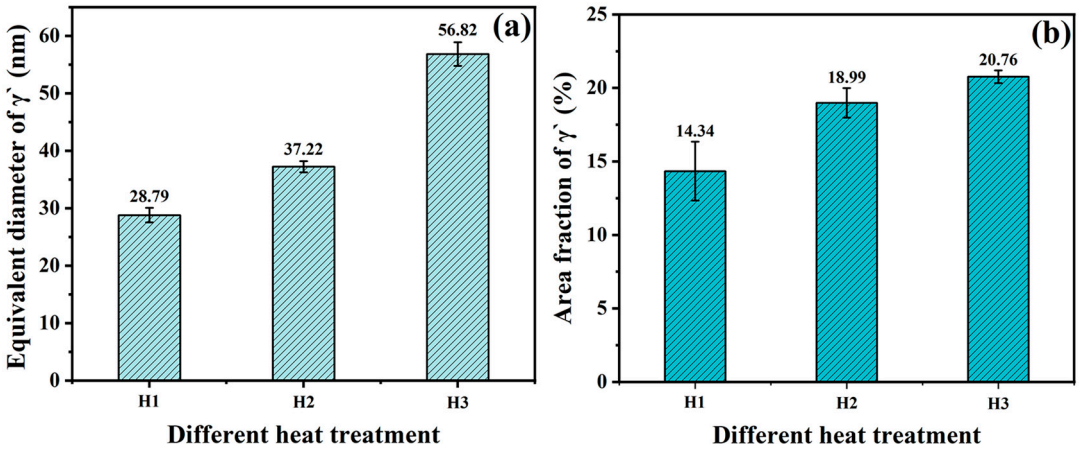

Figure 6. Statistics on the equivalent diameter and area fraction of the primary γ′ phase in the dendrite core: (**a**) equivalent diameter and (**b**) area fraction.

3.2. The Thermophysical Properties with Variation of Microstructure

The thermophysical properties, as functions of temperature for the K439B alloy in three different heat treatment states, are shown in Figure 7. Figure 7a presents that the thermal conductivity (κ) of the K439B alloy after heat treatments is much smaller than that of pure Ni. Additionally, the thermal conductivity of the H1 sample is larger than that of the H2 sample, indicating that the precipitation of the γ′ phase has an important effect on the thermal conductivity of the alloy. The thermal diffusivity (α) of K439B under three different heat treatment conditions positively correlated with temperature, as revealed by Figure 7b. And the heat treatment apparently affects the thermal diffusivity, which is $\alpha_{H1} > \alpha_{H2} > \alpha_{H3}$. There is no significant difference among α_{H1}, α_{H2}, and α_{H3} at temperatures lower than 200 °C, but the difference between the samples gradually increases with the increasing temperature. The variation of the average thermal expansion coefficient (α_l) of the three samples is shown in Figure 7c, which is manifested as $\alpha_{lH1} > \alpha_{lH2} > \alpha_{lH3}$. The difference of α_l between the samples gradually increases with the increasing temperature and approaches 0 at 900 °C. The specific heat capacity (C) of both H1 and H3 specimens increases with the temperature rising on the whole, as shown in Figure 7d, and the H3 alloy has a higher slope above 600 °C, showing an accelerating rising trend. Additionally, there exists a turning point at 700 °C–800 °C in the specific heat capacity curve of the H1 specimen. The value of C first decreases at 600 °C, followed by a rapid rise at 800 °C.

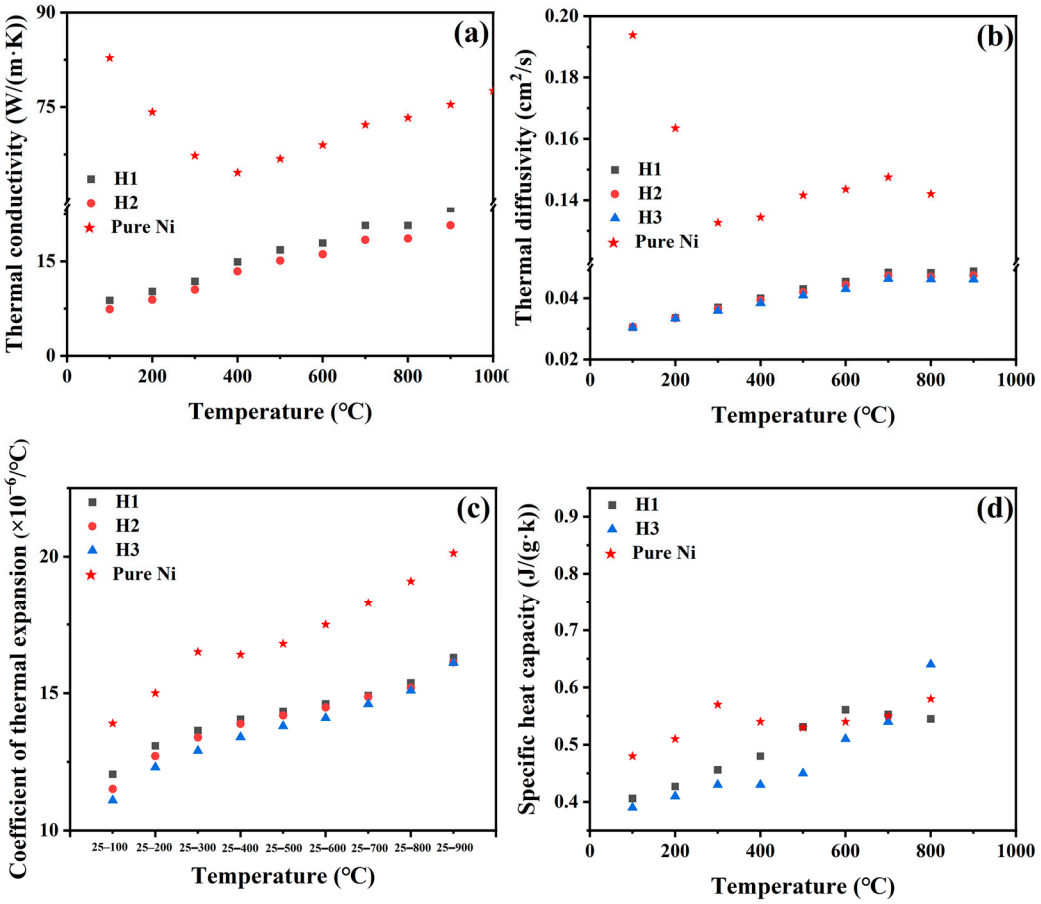

Figure 7. Thermophysical parameters of samples with different heat treatment: (**a**) thermal conductivity; (**b**) thermal diffusivity; (**c**) average thermal expansion coefficient; and (**d**) specific heat capacity. The thermophysical property data for pure nickel are adapted from references [20–22].

It is noteworthy from Figure 7 that all the curves of thermal conductivity, thermal diffusion, average thermal expansion coefficient, and the specific heat capacity of the K439B alloy subjected to different heat treatment processes show an upward trend with the increasing temperature. All four thermophysical parameters increase sharply at 700–800 °C, which indicates that the mean free path of electrons and phonons as thermal carriers of the alloy increases sharply, and this may result in structural destabilization due to the increased thermal activation of electrons and phonons. This provides new corroboration of the alloy's service capability from a physical property perspective.

4. Discussion

4.1. Relationship between Microstructure and Heat Transfer

It is generally believed that the thermophysical properties of alloys mainly depend on the physical properties of the elemental composition [23], and the effect of the microstructure on the thermophysical properties is often not taken into consideration seriously. The thermal conductivity (κ) of an alloy generally consists of two components [24,25]

$$\kappa = \kappa_e + \kappa_p \quad (1)$$

where κ_e is defined as the thermal conductivity generated by the diffusion of free electrons, which will diffuse from the high temperature region to the low one, driven by a temperature gradient to complete the heat transfer process. κ_e and the conductivity σ of the material are closely linked, and the relationship satisfies the Wiedemann–Franz law [25]:

$$\kappa_e = L\sigma T \quad (2)$$

where L is the Lorenz constant and the value is 2.44 × 10^{-8} WΩK^{-2} [25,26]. κ_e is proportional to σ, deduced easily from the Equation (2). The second part, κ_p of κ, is the phonon thermal conductivity formed by the phonons as the thermal conductive carriers, which is the collective motion pattern of lattice in solid materials and independent of the conductivity. κ_p satisfies the following equation [24,25]:

$$\kappa_p = \frac{1}{3} C_v l v \tag{3}$$

where C_v is the volumetric specific heat capacity, l is the mean free path of phonon, and v is the velocity of phonon propagation. A material with a large specific heat capacity conducts more heat driven by the same temperature gradient. Moreover, the greater the mean free path of the phonon, i.e., the less scattering the phonon receiving in motion, the easier the heat conduction will be. And the process of heat conduction will be obviously easier with a faster propagation speed of the phonons. Taking defects and scattering between phonons into account, the phonon thermal conductivity of common metals above room temperature can be well represented by the following expression [24,25,27]:

$$\kappa_p = \frac{1}{\mathrm{A} + BT^n}, \ (0.5 < n < 1) \tag{4}$$

where A and B are constants, and account for defect and scattering between phonons. It is clear that the κ_p initiated by lattice vibrations decreases with increasing temperature, attributed to the increased scattering of interactions between phonons and between phonons and defects at higher temperatures.

Combing the Formulas (1), (2), and (4), the relationship between thermal conductivity and temperature can be obtained:

$$\kappa = L\sigma T + \frac{1}{\mathrm{A} + BT^n}, \ (0.5 < n < 1) \tag{5}$$

From Equation (5), it can be seen that whether the thermal conductivity increases with increasing temperature depends on whether electron or phonon contribution dominates. For pure metals, κ_e is about 20 times as large as κ_p. Hence, the dominant mechanism of heat transfer for pure metals is κ_e, showing a high thermal conductivity. For instance, the thermal conductivity of pure Ni in Figure 6a increases with temperature, because κ_e of pure metals is much larger than κ_p, resulting in the second term on the right in Equation (5) being neglected. Thus, κ of pure Ni is positively correlated with temperature. For alloys, solute atoms dissolving inside the matrix will cause lattice distortion, which leads to a strong scattering effect on the transport behavior of free electrons so that κ_e is greatly reduced. Therefore, the thermal conductivity of alloys is characterized by a joint contribution of phonons and electrons. In Ni-based superalloys, the conductivity of the γ phase is higher than that of the γ′ phase [17,28], and the κ_e in the matrix is greater than that in the γ′ phase. Hence, more γ′ phases account for a smaller κ_e. On the one hand, the mean free path of the electrons in the alloy is much smaller than the size of the γ′ phase, so the scattering of the electrons for conduction at the interface between the γ and γ′ phases should be negligible. On the other hand, the size of the γ′ phase is comparable to, or slightly smaller than, that of the phonons, indicating that the size of the γ′ phase has a great impact on the κ_p [29]. In summary, the effect of the γ′ phase size on κ_p will be greater. In addition, the formation and growth of the γ′ phase usually brings about the precipitation of solute atoms from the γ matrix, which can lead to a reduction in lattice distortion. Thus, for alloys with fixed compositions, the process of precipitate nucleation and growth will lead to an increase in the corresponding κ_e value to a certain extent. The thermal conductivity of the K439B alloy increases with the rising temperature, indicating that electrons dominate over phonons in contributing to thermal conductivity. This contribution can be observed more clearly in Figure 6b, where the three curves of thermal diffusivity gradually plateau

between 800 and 900 °C. This suggests that the factors influencing thermal conductivity shift completely from electron dominance to phonon control at high temperatures. The rise, flattening, or fall at the end of these three curves directly correlates with the distribution of the γ' phase [30,31]. The influence of κ_p in specimens treated with H2 and H3 will be greater than in those treated with H1 due to the larger size and volume fraction of the γ' phase in these specimens. Therefore, the thermal diffusion coefficient corresponding to the same temperature will show a more significant decrease.

From the perspective of microscopic heat transfer analysis, there are two types of interfacial thermal resistances in the K439B alloy. One is the resistance between the γ' phase and the γ phase matrix, and the other is among the grain boundaries. Additionally, the presence of more $M_{23}C_6$ carbides at the grain boundaries influences the alloy's thermal conductivity. The increase in both the interface between the dendrite core and interdendritic region, as well as the size and volume fraction of the γ' phase, contributes to a reduction in κ_p. All of these factors collectively result in a lower thermal conductivity.

In summary, the precipitation of the γ' phase or solute atoms from the matrix can increase κ_e by reducing the scattering of free electrons induced by lattice distortion. However, a greater and larger distribution of γ' phases within the matrix will reduce κ_p to some extent. Additionally, the thermal resistances at both the γ/γ' interface and grain boundaries, as well as the presence of carbides [19], contribute to a lower thermal conductivity. All these factors ultimately lead to a reduction in the thermal conductivity of the aged alloys.

4.2. Influence of Microstructure on Thermal Expansion and Specific Heat Capacity

The coefficient of thermal expansion is the relative change in length or volume that occurs in a solid for every 1 °C rise in temperature. Therefore, even if the composition in the substance is the same, different structures can cause different coefficients of thermal expansion. Compared with H1, more solute atoms precipitated from the matrix to form the γ' phase and $M_{23}C_6$ carbides after H2 and H3 treatment. This resulted in a decrease in the disorder of the chemical composition in the matrix γ phase, and a reduction in lattice distortion, while simultaneously decreasing the corresponding solid-solution strengthening ability. The ordered structural γ' phase has a lower coefficient of thermal expansion than the matrix γ phase [28] due to stronger interatomic bonding forces of the γ' phase, this results in a tighter and more organized atomic arrangement. After H2 and H3 heat treatments, the size and volume fraction of the γ' phase are obviously increased, which leads to lower average linear expansion coefficients of these two specimens. It demonstrates that the modulation of the thermal expansion coefficient can be achieved by changing the relative volume fractions of ordered and disordered solid solution states in the alloy microstructure.

The coefficient of thermal expansion represents the relative change in length or volume that occurs in a solid for every 1 °C rise in temperature. Therefore, even with the same composition, different microstructures of alloys can result in different coefficients of thermal expansion. Compared to H1, H2 and H3 treatments led to more solute atoms precipitating from the matrix to form γ' phases and $M_{23}C_6$ carbides. This reduced the disorder of the chemical composition in the γ matrix, minimized lattice distortion, and correspondingly decreased the solid solution strengthening ability. The ordered γ' phase has a lower coefficient of thermal expansion than the γ matrix [32], which can be attributed to stronger interatomic bonding forces resulting in a tighter and more organized atomic arrangement. After H2 and H3 heat treatments, the size and volume fraction of the γ' phase noticeably increased, resulting in lower average linear expansion coefficients for these two specimens. This demonstrates that adjusting the relative volume fractions of the γ' phase in the alloy can modulate the thermal expansion coefficient.

The specific heat capacity curve of the alloy under the H1 heat treatment condition in Figure 7d initially decreases after 600 °C and then rises rapidly upon reaching 800 °C, which is a trend closely associated with microstructural changes. According to the heat treatment process, the specimen treated with H1 primarily comprises γ phases in a supersaturated solid solution state, as its heat treatment is held at a temperature higher than the γ' phase

dissolution temperature, despite the presence of a tiny γ' phase precipitation during the solidification process. During the specific heat capacity test, the γ' phase precipitates from the supersaturated γ phase upon heating to 600 °C. Since the energy of the metastable microstructure is relatively high, the specimen needs to release heat to transform into the stable state, so less heat is required to raise the temperature of the superalloy, which leads the heat capacity temperature to curve downward. This phenomenon may explain the decrease in the specific heat capacity observed in the temperature range from 600 °C to 800 °C. Additionally, the determination of the specific heat capacity is not very accurate due to fluctuations in the signal (especially at higher temperatures, above 700 °C). Further repetitive measurements as well as narrowing down the temperature interval of the measurements are needed to verify speculations.

5. Conclusions

The change in the thermophysical parameters of the K439B equiaxial cast Ni-based superalloy was studied within the temperature range from 100 °C to 900 °C. The effects of the microstructural features on the thermophysical properties were analyzed, and the main conclusions drawn are as follows:

(1) All the studied thermophysical parameters of the alloys underwent different heat treatments, including thermal conductivity, thermal diffusivity, average linear expansion coefficient, and specific heat capacity, which increases with the rising temperature. These parameters exhibit a significant increase particularly between 700 °C and 800 °C. The increased thermal activation of electrons and phonons is prone to the structural destabilization of the alloy.

(2) The increase in volume fraction and size of the γ' phase results in a decrease in thermal conductivity, thermal diffusion coefficient, average coefficient of linear expansion, and specific heat capacity at the same measurement temperature.

(3) An increase in the volume fraction and size of the γ' phase leads to an increase in the γ/γ' phase interface. Additionally, the increased area of the boundaries between the dendrites also reduces the phonon thermal conductivity, ultimately resulting in a decrease in the thermal conductivity.

(4) The alloys with a 20 h aging treatment exhibit stable thermal conductivity and a low average linear expansion coefficient at temperatures between 800 °C and 900 °C. This combination of properties is conducive to maintaining the thermal stability of the alloy in a high-temperature service environment.

Continued research is needed to eliminate the limitations of the current program, such as the determination of thermophysical properties of an as-cast K439 alloy without heat treatment and the alloy aged at 845 °C for a longer time, and a comparative study of the thermophysical properties of samples from different batches is needed to further demonstrate the generalizability of the conclusions.

Author Contributions: Conceptualization: Y.W. and X.H.; Methodology: Y.W. and J.G.; Validation: Y.W. and J.G.; Formal Analysis: X.Z. and J.Z.; Investigation: X.Z., J.Z. and J.G.; Resources: X.H.; Data Curation: Y.W., X.Z. and J.Z.; Writing—Original Draft Preparation: Y.W. and J.G.; Writing—Review and Editing: Y.W. and X.H.; Visualization: J.G. and Y.W.; Supervision: X.H.; Project Administration: X.H.; and Funding Acquisition: X.H. All authors have read and agreed to the published version of the manuscript.

Funding: This research was supported by the National Science and Technology Major Project of China (No. J2019-VI-0004-0117).

Data Availability Statement: The raw data supporting the conclusions of this article will be made available by the authors on request.

Conflicts of Interest: The authors declare that the research was conducted in the absence of any commercial or financial relationships that could be construed as a potential conflict of interest.

References

1. Gao, J.L.; Zhang, Y.T.H.; Zhu, L.L.; Hu, Q.M.; Hu, J.H.; Zhang, S.Z. Machine learning assisted design of Ni-based superalloys with excellent high-temperature performance. *Mater. Charact.* **2023**, *198*, 112740. [CrossRef]
2. Zelaia, P.F.; Acevedo, O.D.; Kirka, M.M.; Leonard, D.; Yoder, S.; Lee, Y. Creep behavior of a high-γ′ Ni-based superalloy fabricated via electron beam melting. *Metall. Mater. Trans. A-Phys. Metall. Mater. Sci.* **2021**, *521*, 574–590. [CrossRef]
3. Mouritz, A.P. (Ed.) *12—Superalloys for Gas Turbine Engines*; Woodhead Publishing: Sawston, UK, 2012; pp. 251–267.
4. Schafrik, R.E.; Ward, D.D.; Groh, J.R. Application of alloy 718 in GE aircraft engines: Past, present and next five years. In *Superalloys 718, 625, 706 and Various Derivatives*; TMS: Pittsburgh, PA, USA, 2001; pp. 1–11.
5. Reed, R.C. *The Superalloys Fundamentals and Applications*; Cambridge University Press: Cambridge, UK, 2006.
6. Pollock, T.M. Alloy design for aircraft engines. *Nat. Mater.* **2016**, *15*, 809–815. [CrossRef] [PubMed]
7. Chen, J.B.; Chen, J.Y.; Wang, Q.J.; Wu, Y.D.; Li, Q.; Xiao, C.B.; Li, S.L.; Wang, Y.D.; Hui, X.D. Enhanced creep resistance induced by minor Ti additions to a second generation Ni-based single crystal superalloy. *Acta Mater.* **2022**, *232*, 117938. [CrossRef]
8. Rudajevová, A.; Staněk, M.; Lukáč, P. Determination of thermal diffusivity and thermal conductivity of Mg-Al alloys. *Mater. Sci. Eng. A* **2003**, *341*, 152–157. [CrossRef]
9. Rudajevová, A.; Lukáč, P. Comparison of the thermophysical properties of AM20 and AS21 magnesium alloys. *Mater. Sci. Eng. A* **2005**, *397*, 16–21. [CrossRef]
10. Yamasaki, M.; Kawamura, Y. Thermal diffusivity and thermal conductivity of Mg-Zn-rare earth element alloys with long-period stacking ordered phase. *Scr. Mater.* **2009**, *60*, 264–267. [CrossRef]
11. Kumar, R.; Hussainova, I.; Antonov, M.; Maurya, H.S.; Ripoll, M.R. Temperature-induced wear micro-mechanism transition in additively deposited nickel alloys with different solid lubricants. *Wear* **2024**, *552–553*, 205452. [CrossRef]
12. Liu, Z.S.; Li, C.W.; Dong, A.P.; Gu, J.F. Effect of initial microstructure on the properties of K439B Ni-based superalloy during prolonged aging at 800 °C. *Intermetallics* **2024**, *172*, 108364. [CrossRef]
13. Zhang, L.L.; Chen, J.Y.; Tang, X.; Xiao, C.B.; Zhang, M.J.; Yang, Q. Evolution of Microstructures and Mechanical Properties of K439B Superalloy During Long-Term Aging at 800 °C. *Acta Metall. Sin.* **2023**, *59*, 1253–1264.
14. Li, Z.; Zhang, Z.L.; Wu, A.P.; Zhang, M.J.; Kang, J.; Liu, Q.; Zhao, Y.; Chen, J.Y. Microstructure and mechanical properties of laser welded and post-weld heat-treated K439B superalloy. *Trans. Nonferrous Met. Soc. China* **2024**, *34*, 905–917. [CrossRef]
15. Liu, Z.S.; Li, C.W.; Dong, A.P.; Gu, J.F. The precipitation behavior of η phase with lamellar morphology in a newly designed K439B Ni-based superalloy. *Mater. Today Commun.* **2024**, *39*, 108844. [CrossRef]
16. Sun, W.; Qin, X.Z.; Guo, J.T.; Lou, L.H.; Zhou, L.Z. Thermal stability of primary MC carbide and its influenceon the performance of cast Ni-base superalloys. *Mater. Des.* **2015**, *69*, 81–88. [CrossRef]
17. Nagarajan, B.; Castagne, S.; Annamalai, S.; Fan, Z.; Chan, W.L. Effect of Microstructure on Electrical Conductivity of Ni-Base Superalloys. *Metall. Mater. Trans. A* **2017**, *48*, 3745–3757. [CrossRef]
18. Aghaie-Khafri, M.; Hajjavady, M. The effect of thermal exposure on the properties of a Ni-base superalloy. *Mater. Sci. Eng. A* **2008**, *487*, 388–393. [CrossRef]
19. Cui, L.Q.; Yu, J.J.; Liu, J.L.; Sun, X.F. Microstructural evolutions and fracture behaviors of a newly developed Ni-base superalloy during creep deformation. *J. Alloys Compd.* **2018**, *746*, 335–349. [CrossRef]
20. Touloukian, Y.S.; Ho, C.Y. *Properties of Selected Ferrous Alloying Elements*; CINDAS Data Series on Material Properties, Volume III-1; McGraw-Hill: New York, NY, USA, 1981.
21. Gray, D.E. *American Institute of Physics Handbook*; McGraw-Hill: New York, NY, USA, 1957.
22. Yang, S.M.; Tao, W.Q. *Heat Transfer Theory*; Higher Education Press: Beijing, China, 2006.
23. Quested, P.N.; Brooks, R.F.; Chapman, L.; Morrell, R.; Youssef, Y.; Mills, K.C. Measurement and estimation of thermophysical properties of Ni-based superalloys. *Mater. Sci. Technol.* **2009**, *25*, 154–162. [CrossRef]
24. Klemens, P.G.; Williams, R.K. Thermal conductivity of metals and alloys. *Int. Met. Rev.* **1986**, *31*, 197–215. [CrossRef]
25. Grimvall, G. *Thermophysical Properties of Materials (Enlarged and Revised Edition)*; Elsevier Science B.V.: Amsterdam, The Netherlands, 1986.
26. Kim, H.; Gibbs, Z.M.; Tang, Y.L.; Wang, H.; Snyder, G.J. Characterization of Lorenz number with Seebeck coefficient measurement. *APL Mater.* **2015**, *3*, 041506. [CrossRef]
27. Tritt, M. *Thermal Conductivity, Theory, Properties and Applications*; K luwer Academic/PlenumPublishers: New York, NY, USA, 2004.
28. Roebuck, B.; Cox, D.; Reed, R. the temperature dependence of γ‘ volume fraction in a Ni-based single crystal superalloy from resistance measurements. *Scr. Mater.* **2001**, *44*, 917–921. [CrossRef]
29. Miura, A.; Osada, T.; Kawagishi, K.; Uchida, K. Thermal transport properties of Ni–Co-based superalloy. *AIP Adv.* **2020**, *10*, 125118. [CrossRef]
30. Mills, K.C.; Youssff, Y.M.; Li, Z.S. The effect of aluminium content on thermophysical properties of ni-based superalloys. *ISIJ Int.* **2006**, *46*, 50–57. [CrossRef]

31. Mills, K.C.; Youssff, Y.M.; Li, Z.S.; Su, Y.C. Calculation of thermophysical properties of Ni-based superalloys. *ISIJ Int.* **2006**, *46*, 623–632. [CrossRef]
32. Cheng, S.H.; Qin, X.Z.; Wen, B.; Wang, J.Q.; Wu, Y.S.; Zhou, L.Z. Effects of Al and Ti on thermal expansion behavior of a Ni–Fe–Cr-based superalloy: A combined experimental and first-principle study. *J. Mater. Res. Technol. JMRT* **2024**, *29*, 3805–3812. [CrossRef]